Asian Journal of Chemistry; Vol. 38, No. 2 (2026), 491-498
ASIAN JOURNAL OF CHEMISTRY
https://doi.org/10.14233/ajchem.2026.35092

Green Synthesis of Ni-Fe co-doped TiO_2 ($Ni_{0.05}Fe_{0.05}Ti_{0.9}O_2$) Nanoparticles for Enhanced Supercapacitor Applications

E. KRISHNAKANTH[1,] and P. MOHAN KUMAR[2,*,]

[1]Material Research Centre, School of Engineering, Presidency University, Bangalore-560064, India
[2]Department of Physics, School of Engineering, Presidency University, Bangalore-560064, India

*Corresponding author: E-mail: mohankumar.p@presidencyuniversity.in

Received: 17 October 2025 *Accepted*: 15 January 2026 *Published online*: 31 January 2026 AJC-22268

This work reports the green synthesis of Ni and Fe co-doped TiO_2 nanocomposites *via* solution combustion using aloe vera gel as bio-fuel. The prepared $Ni_{0.05}Fe_{0.05}Ti_{0.9}O_2$ composition was confirmed by XRD and Raman spectroscopy, which showed anatase phase retention and successful substitution of Ti^{4+} by Ni^{2+} and Fe^{3+}, inducing lattice distortion and local symmetry defects. SEM revealed reduced particle size and improved dispersion due to co-doping. Electrochemical studies including cyclic voltammetry, galvanostatic charge–discharge and impedance spectroscopy demonstrated enhanced capacitance, energy density and charge transfer dynamics in $NiFeTiO_2$ compared to pure and Fe-doped TiO_2. The $NiFeTiO_2$ electrode achieved a high specific capacitance (140 F g^{-1}), energy density (280 Wh/kg) and power density (54 kW/kg), highlighting the complementary role of binary doping in improving conductivity and pseudocapacitive behaviour. Overall, green synthesis and transition metal co-doping offer a sustainable route to high-performance supercapacitor electrode materials.

Keywords: Green synthesis, Aloe Vera, Energy storage, Supercapacitor.

INTRODUCTION

The energy demand has increased in pace with the spread of technological advancements. A new energy demand is emerging and this makes way for new-generation energy storage systems as well as renewable (convertible) energy sources [1,2]. On the other hand, the transportation of such renewable energy from the generation point to the application point is still another troublesome job. Therefore, the development of high-performance, high-capacity and stable energy storage devices has been drawn a great deal of attention as one of the most promising solutions. Tremendous progresses of energy storage devices including conventional capacitors and batteries have been already made all over the world. However, the commercial applications are still behind the global demand [3-5]. Under this circumstance, the full growth of energy storage systems (ESS) emerges as a major theme being pursued by a legion of scientific experts and second-generation lithium-ion batteries (LiB), fuel cells, dielectric capacitors and supercapacitors (SC) are four prevalent examples owing to their high specific energy, power density, high sustainability, long cyclic life and low environmental impact [6-9].

In recent years, electrochemical research has attracted considerable interest owing to growing concerns over energy and environmental challenges, electrochemical investigations have become increasingly prominent. Since its discovery [10, 11], TiO_2 has been extensively used in applications like battery photo-anodes, water splitting, supercapacitors and dye removal. With its high surface area and sturdy framework, nanostructured TiO_2 NPs shows promising application in both electrical double-layer and pseudocapacitive supercapacitors. Still, its wide band gap (~3.0-3.2 eV) and naturally low conductivity limit its electrochemical efficiency [12,13]. These factors result in low faradaic activity and elevated internal resistance, ultimately restricting its capacitance and energy output. Therefore, boosting the electrochemical behaviour of TiO_2 is key for advancing its role in supercapacitor devices.

A highly effective approach to addressing the limitations of TiO_2 involves doping with transition metals. Introducing metal ions can create additional energy states [14,15], increase the density of charge carriers and induce defect sites particularly oxygen vacancies that helps to reduce the band gap and enhance electrical conductivity. For instance, Ni^{2+} and Fe^{3+} ions can replace Ti^{4+} within the TiO_2 crystal lattice, generating localised gap states that improve conductivity [16,17]. Studies

have demonstrated that Ni doping helps stabilise the anatase phase of TiO_2, decreases its band gap and increases both conductivity and the number of active sites. Likewise, Fe doping lowers TiO_2's band gap from 3.1 eV to approximately 2.8 eV as the iron concentration increases, due to Fe^{3+} energy levels overlapping with the conduction band [18,19]. This reduction in band gap through Ni or Fe doping enhances electrical conductivity and expands redox activity, similar to the effects observed when TiO_2 is hydrogenated, which introduces Ti^{3+} states and structural disorder to boost conductivity and pseudo-capacitance. Beyond individual dopants, co-doping TiO_2 with both Ni and Fe can produce synergistic effects. co-Doping typically induces more substantial modifications in both the structural and electronic characteristics of TiO_2 compared to single-element doping. The simultaneous presence of Ni^{2+}/Ni^{3+} and Fe^{2+}/Fe^{3+} redox pairs introduce multiple active sites and promotes the formation of oxygen vacancies, enhancing charge transfer dynamics and supporting increased pseudo-capacitive behaviour.

From an electrochemical standpoint, Ni/Fe co-doped TiO_2 benefits from both electrical double-layer capacitance and Faradaic pseudo capacitance. The incorporated Ni and Fe ions introduce additional redox-active centres, supplementing the inherently limited $Ti^{4+} \rightleftharpoons Ti^{3+}$ redox couple, thereby enhancing charge storage capabilities [20]. The redox pairs Ni^{2+}/Ni^{3+} and Fe^{2+}/Fe^{3+} contribute actively during charge-discharge cycles, leading to improved specific capacitance and an extended potential window. Furthermore, the co-doping reduces the band gap, increasing electronic conductivity and lowering equivalent series resistance (ESR), which facilitates high-rate cycling. The integration of green, plant-assisted synthesis further enables precise control over nanostructure and phase composition in an environmentally responsible manner. For the first time, Ni and Fe co-doped TiO_2 nanoparticles were successfully prepared through a solution combustion technique. The study revealed a notable enhancement in electrochemical behaviour, with the interpretation of results provided herein.

EXPERIMENTAL

Preparation of Ni and Fe co-doped TiO_2 NPs: A solution combustion route was employed to synthesise nanocomposites of TiO_2, Fe and Ni, using aloe vera gel as a green fuel source [21]. For this method, 20 mL of freshly extracted aloe vera gel was blended with 80 mL of deionised water and then filtered to extract the required gel. This filtered gel was used as fuel in the combustion process. To obtain a final composition of $Ni_{0.05}Fe_{0.05}Ti_{0.9}O_2$, the precursor salts-titanium(IV) isopropoxide, ferric nitrate nonahydrate and nickel(II) nitrate hexahydrate (all compounds, with a purity of 99.99%, Sigma-Aldrich) were precisely added into silica crucible, provided with 10 mL of aloe vera gel. After thorough mixing with a magnetic stirrer for 30 min, the crucibles were placed inside a muffle furnace pre-set to 450 ± 10 ºC. The exothermic reaction initiated combustion, which finished within 15 min, yielding the nanocomposites. Finally, the products underwent calcination at 500 ºC for 3 h.

Characterisation: As prepared TiO_2, Fe-doped TiO_2, Ni and Fe co-doped TiO_2 nanoparticles were characterised to understand their structural, morphological and electrochemical features. Structural analysis was carried out using X-ray diffraction (Bruker D2 Phaser) was used to study the structural phases, while surface morphology was analysed by scanning electron microscopy (SEM-EDX, ZEISS). Raman spectroscopy was conducted using an (Enspectra Raman microscope) and electrochemical measurements were performed with a CHI608E electrochemical workstation.

RESULTS AND DISCUSSION

Identification of phase structure and crystallite size: Fig. 1 displays the XRD results of Ni and Fe co-doped TiO_2, which were utilised to analyse structural features, phase composition and lattice parameters of the sample. XRD analysis revealed distinct peaks at 25.18º, 36.03º, 37.94º, 48.06º, 54.13º, 55.18º, 62.63º, 68.92º, 70.30º and 75.10º matching the (101), (103), (004), (200), (105), (211), (204), (116), (220) and (215) planes of anatase TiO_2 (JCPDS No. 21-1272) respectively [22-24]. Due to the close similarity in ionic radii among Ti^{4+}, Fe^{3+} and Ni^{2+}, no separate iron or nickel oxide phases were observed in the XRD patterns. This implies that Fe^{3+} and Ni^{2+} ions were incorporated into the TiO_2 structure by substituting Ti^{4+} sites [25,26]. Furthermore, ICDD reference id 00-041-0214 confirms the formation of iron nickel titanium oxide and the variation of peak intensity, slight peak shift confirms the addition of dopants.

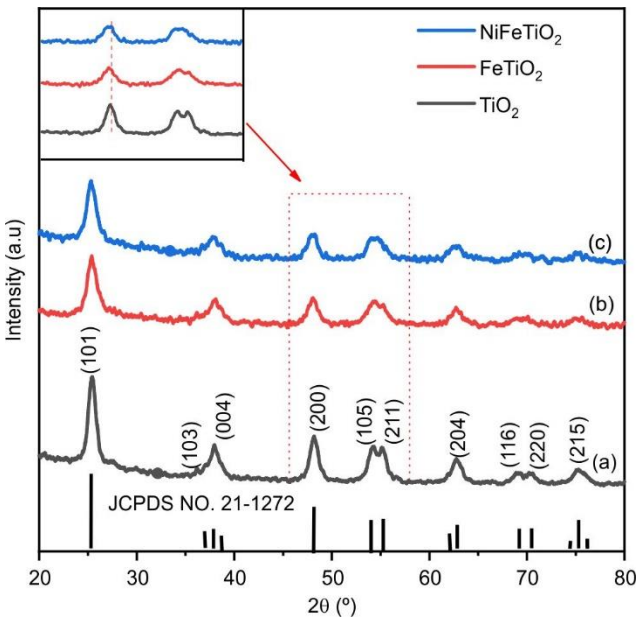

Fig. 1. XRD patterns of Graphic representation of TiO_2, Fe doped TiO_2, Ni and Fe co-doped TiO_2 NPs

The crystallite size and structural characteristics of Ni and Fe co-doped TiO_2 were examined using Scherrer's equation and the Williamson-Hall (W-H) method. The crystallite size can be calculated using the Scherrer equation as follows:

$$D = \frac{K\lambda}{\beta \cos\theta} \quad (1)$$

where D stands for the crystallite size; λ is the wavelength of Cu*K*α radiation (1.5406 Å); β indicates the full width at half maximum of diffraction peak; K is a shape factor (0.94) and θ represents the diffraction angle at the peak maximum. The corresponding lattice parameters were computed using the following set of equations:

$$D_{(hkl)} = \frac{\lambda}{2\sin\theta} \quad (2)$$

$$\frac{12}{d_{(hkl)}} = \frac{h^2 + k^2}{a^2} + \frac{l^2}{c^2} \quad (3)$$

The term $d_{(hkl)}$ refers to the distance between atomic planes indexed by (*hkl*), λ is the wavelength of the X-ray used, θ is the corresponding diffraction angle and (*hkl*) indicates the specific set of lattice planes. For anatase-phase TiO_2, the crystal system is tetragonal with equal a and b parameters, while *c* is distinct ($a = b \neq c$) [26]. The crystallite sizes and lattice parameters for Ni and Fe co-doped TiO_2 nanoparticles are summarised in Table-1, reveal a noticeable decrease in crystallite size with the incorporation of dopant ions.

TABLE-1
CRYSTAL SIZES OF TiO_2, Fe DOPED TiO_2, Ni AND Fe co-DOPED TiO_2 NPs

Sample	Crystal size (nm)	
	Scherrer's	W-H
TiO_2	8.18	6.91
$FeTiO_2$	7.27	4.30
$NiFeTiO_2$	7.14	3.73

Raman analysis of Ni and Fe co-doped TiO_2: The Raman spectral changes reflect factors such as non-stoichiometry, structural imperfections, phase variations and bond structure modifications [27]. Fig. 2 illustrates the Raman spectra of pure TiO_2, Fe doped TiO_2, Ni and Fe co-doped TiO_2 samples, all samples exhibit six prominent Raman-active vibrational modes: E_g (146.27 cm^{-1}), E_g (196.11 cm^{-1}), B_{1g} (396.52 cm^{-1}), A_{1g} + B_{1g} (515.13 cm^{-1}) and E_g (640.31 cm^{-1}), which are characteristic of the anatase of TiO_2. The presence of these modes confirms the retention of the anatase crystal structure across all compositions [28,29]. The Raman E_g mode centred at 145 cm^{-1} showed a marginal shift to higher wavenumbers and reduction in intensity, as shown in Fig. 2. This observed shift and intensity change suggest the formation of structural defects, attributed to the substitution of Ti^{4+} by Ni^{2+} and Fe^{3+} in the host lattice. These observations are in good agreement with XRD results.

Surface morphology: Scanning electron microscopy (SEM) was employed to examine the surface morphology of the samples and the results are shown in Fig. 3, providing a comparative analysis of pure TiO_2 (a-b), Fe-doped TiO_2 (c-d) and Ni and Fe co-doped TiO_2 (e-f) nanostructures. At low magnification (Fig. 3a), the TiO_2 sample displays irregular, aggre-gated particles forming loosely bound microstructures. The high-magnification image (Fig. 3b) reveals densely packed, nanocrystalline particles with an average size of 146.5 nm, after incorporation of Fe as a dopant (Fig. 3c-d) leads to noticeable changes in morphology. At low magnification (Fig. 3c),

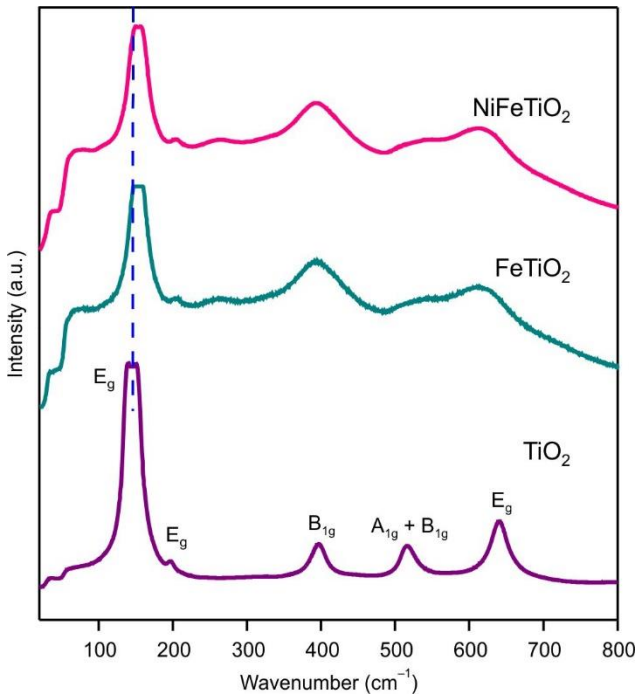

Fig. 2. Raman spectra of Graphic representation of TiO_2, Fe doped TiO_2, Ni and Fe co-doped TiO_2 NPs

Fe doped TiO_2 displays smaller, more spherical particles with reduced agglomeration. High-magnification imaging (Fig. 3d) indicates an average particle size of approximately 144.3 nm. The co-doping of TiO_2 with Ni and Fe (Fig. 3e-f) results in pronounced morphological refinement. Low-magnification SEM imagery (Fig. 3e) reveals a microstructure consisting of finely dispersed secondary clusters, in contrast to the dense agglomerates observed in pure TiO_2. The high-magnification image (Fig. 3f) confirms a significant decrease in particle size, with an average of 85.41 nm. This reduction in crystallite size and improved particle dispersion are likely due to the synergistic effect of Ni and Fe ions disrupting lattice continuity, This SEM analysis reveals a structural evolution marked by reduced particle agglomeration and improved nanoscale uniformity, which correlates strongly with improved electrochemical behaviour. Fig. 3g,h,i displays EDX results, which serve as a crucial analytical technique for determining the elemental composition of the materials. The spectra confirm the presence and distribution of Ni and Fe in the co-doped TiO_2 and provide the corresponding weight percentages of each element.

Electrochemical studies: Electrochemical evaluations such as cyclic voltammetry (CV), galvanostatic charge-discharge (GCD) and electrochemical impedance spectroscopy (EIS) were conducted to assess the electrochemical behaviour of the fabricated electrodes [30-32]. These experiments were performed using a CHI608E electrochemical workstation within a conventional three-electrode system including a working electrode, an Ag/AgCl reference electrode and a platinum counter electrode with 1 M Na_2SO_4 aqueous solution acting as electrolyte. All the pure TiO_2, Fe doped TiO_2, Ni and Fe co-doped TiO_2 samples were loaded with an active material mass of about 0.022 g. Cyclic voltammograms were obtained at various scan rates (10-50 mV/s) using a 1 M Na_2SO_4 elect-

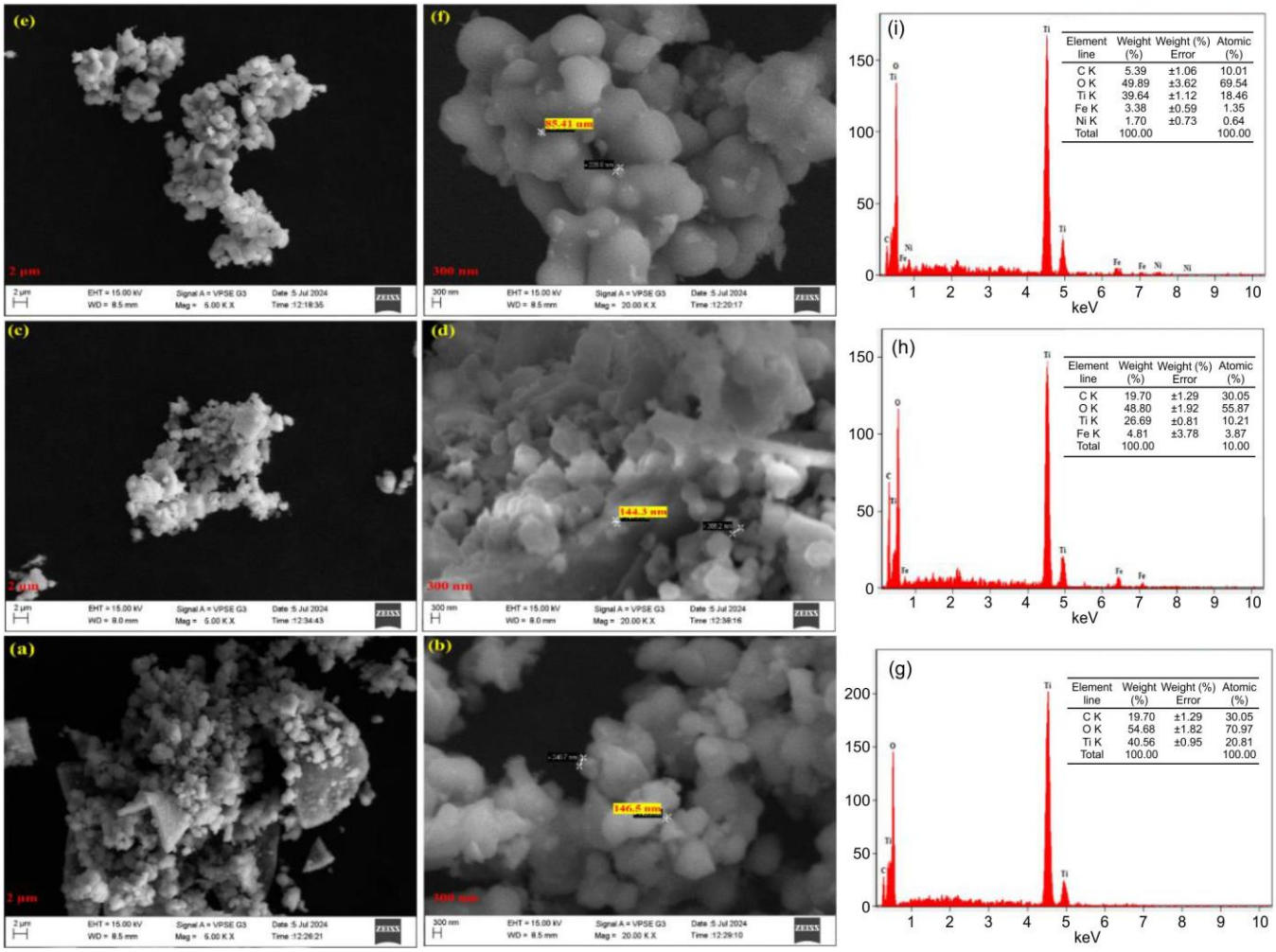

Fig. 3. Surface morphology and EDX spectra of TiO_2 (a, b, g), Fe doped TiO_2 (c, d, h), Ni and Fe-co doped TiO_2 (e, f, i) NPs

rolyte and the observed redox behaviour aligns well with the previously reported studies [33].

Cyclic voltammetry studies: As shown in Fig. 4a-c, the cyclic voltammograms of pure TiO_2, Fe doped TiO_2, Ni and Fe co-doped TiO_2 demonstrate a direct relationship between scan rate and current. The observed symmetry of the CV curves indicates good reversibility in redox reactions. Furthermore, with increasing scan rate, the redox peaks exhibit a shift-oxidation peaks moving to higher potentials and reduction peaks to lower-suggesting diffusion-limited kinetics. An enlarged CV area at lower scan rates in doped samples reflects enhanced charge storage, contributing to improved specific capacitance. The nature of this response suggests that the electrode combines pseudo-capacitance with double-layer capacitance, resulting in capacitor-like behaviour which is highly desirable for energy storage applications [34].

To better understand the charge retention mechanism, the log peak current (I_p) against log scan rate (V) is plotted, which yielded a straight-line relationship, as seen in Fig. 5a-c. A slope of 1 indicates ideal capacitive behaviour, while a slope of 0.5 represents a diffusion-controlled process. Intermediate slopes (0.5-1) point to a combination of both mechanisms. The extracted b-values for TiO_2, Fe-doped TiO_2, Ni and Fe co-doped TiO_2 (Table-2) fall within this range, confirming a hybrid storage mechanism. To isolate and quantify these contributions, we plotted $V^{0.5}$ *versus* $I/V^{0.5}$ as depicted in Fig. 5d-f. The slope and intercept of the fitted line represent k_1 (capacitive) and k_2 (diffusion-controlled) respectively. As specified in Table-2, the consistent observation that $k_1 < k_2$ confirms that the dominant mechanism is diffusion-controlled. Also, the increasing trend in k_2 with adding dopants with TiO_2 underscores a growing preference towards diffusion-based energy storage.

TABLE-2
CONSTANTS (b, k_1, k_2) AND WARBURG COEFFICIENT DATA OF TiO_2, Fe DOPED TiO_2, Ni AND Fe co-DOPED TiO_2 NPs

Samples	b	k_1	k_2	σ (ω)
TiO_2	0.7218	7.14×10^{-18}	3.74×10^{-17}	1333
Fe doped TiO_2	0.5102	4.90×10^{-15}	2.68×10^{-15}	1268
Ni and Fe co-doped TiO_2	0.5110	3.40×10^{-15}	1.86×10^{-15}	511

Electrochemical impedance spectroscopy (EIS): As illustrated in Fig. 6a,c,e, the Nyquist plots for TiO_2, Fe doped TiO_2, Ni and Fe co-doped TiO_2 reveal high-frequency semi-circles representing solution resistance (R_s) and low-frequency lines associated with Warburg diffusion. Upon doping, these

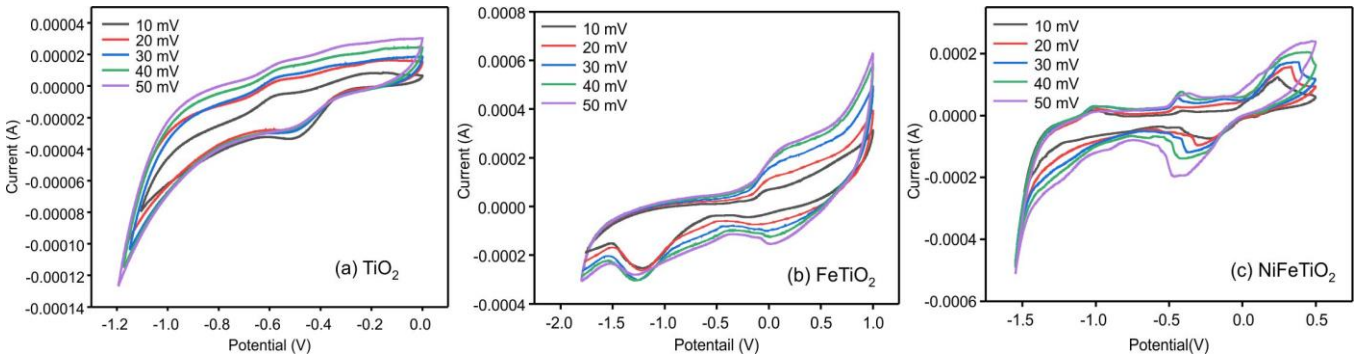

Fig. 4. CVs of TiO_2, Fe doped TiO_2, Ni and Fe co-doped TiO_2 NPs at the scan rates of 10-50 mV s^{-1}

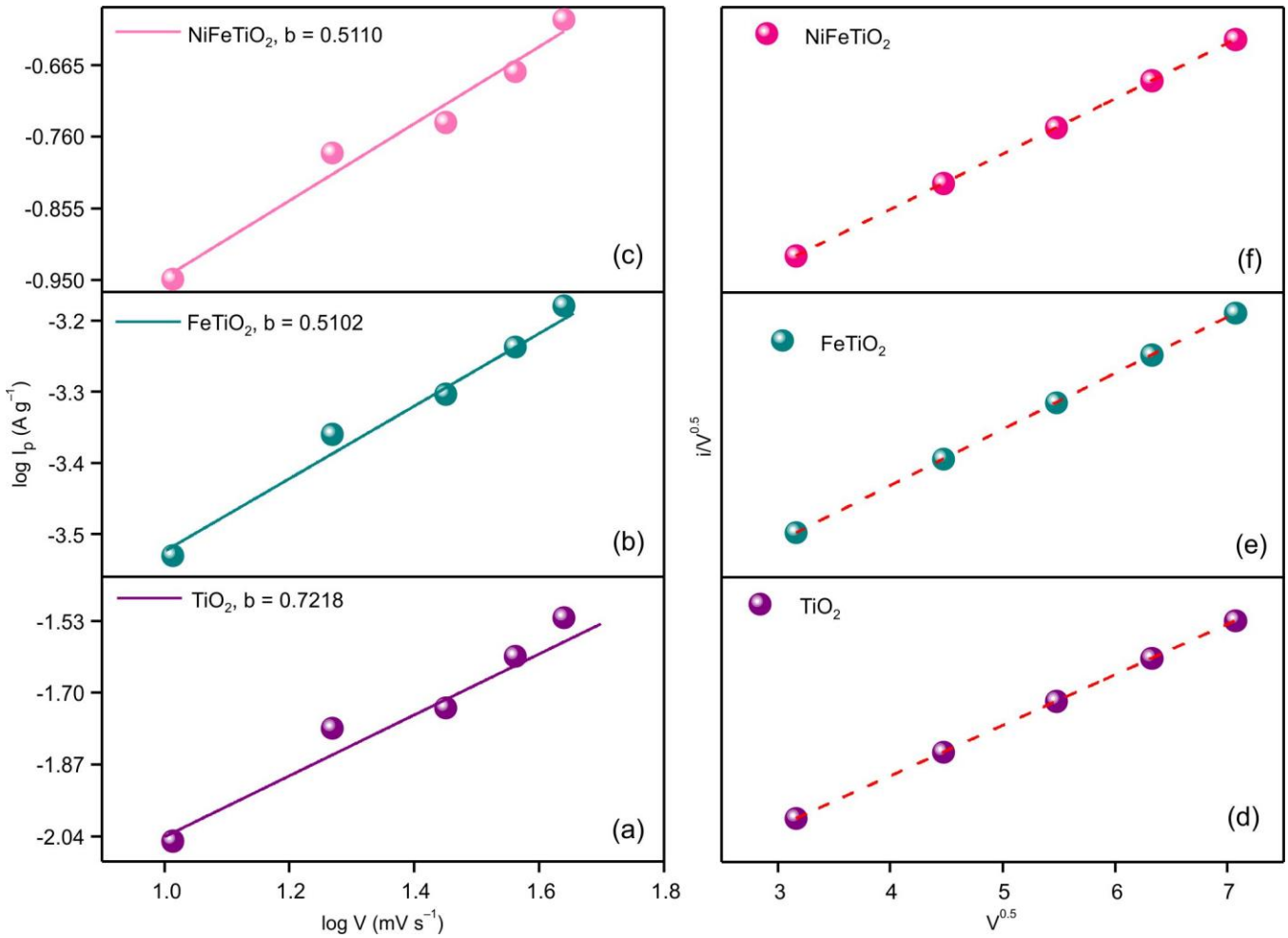

Fig. 5. (a-c) Plots of log I_p *vs.* log V and (d-f) Plots of $i/V^{0.5}$ *vs.* $V^{0.5}$ of TiO_2, Fe-doped TiO_2, Ni and Fe co-doped TiO_2 NPs

plots shift to higher frequencies, indicating improved ionic movement, better electrode-electrolyte contact and lowered surface resistance. Fig. 6b,d,f presents the Warburg coefficients, derived from the slope of Z′ *versus* $\omega^{-1/2}$, which describe the ion transport behaviour. The significantly lower σ value for $NiFeTiO_2$ suggests superior diffusion of ions compared to $FeTiO_2$ and pure TiO_2. This is attributed to enhanced conductivity and better ion accessibility due to co-doping. The reduced semi-circular arc in the $NiFeTiO_2$ impedance spectrum further confirms its lower charge transfer resistance. In contrast, $FeTiO_2$ and TiO_2 show higher σ values and less defined arcs, indicative of higher resistance and slower ion dynamics. Therefore, $NiFeTiO_2$ demonstrates better electrochemical kinetics, making it a more efficient material for applications such as supercapacitors and batteries.

Galvanostatic charge-discharge (GCD): Galvanostatic charge-discharge (GCD) tests were performed on TiO_2, Fe doped TiO_2, Ni and Fe co-doped TiO_2 nanoparticles over a potential range from -1 V to 1 V at a constant current density of 3 mA g^{-1}, as depicted in Fig. 7. The resulting triangular GCD profiles indicate a highly reversible charge/discharge behaviour, typical of capacitive materials. The extended discharge dura-

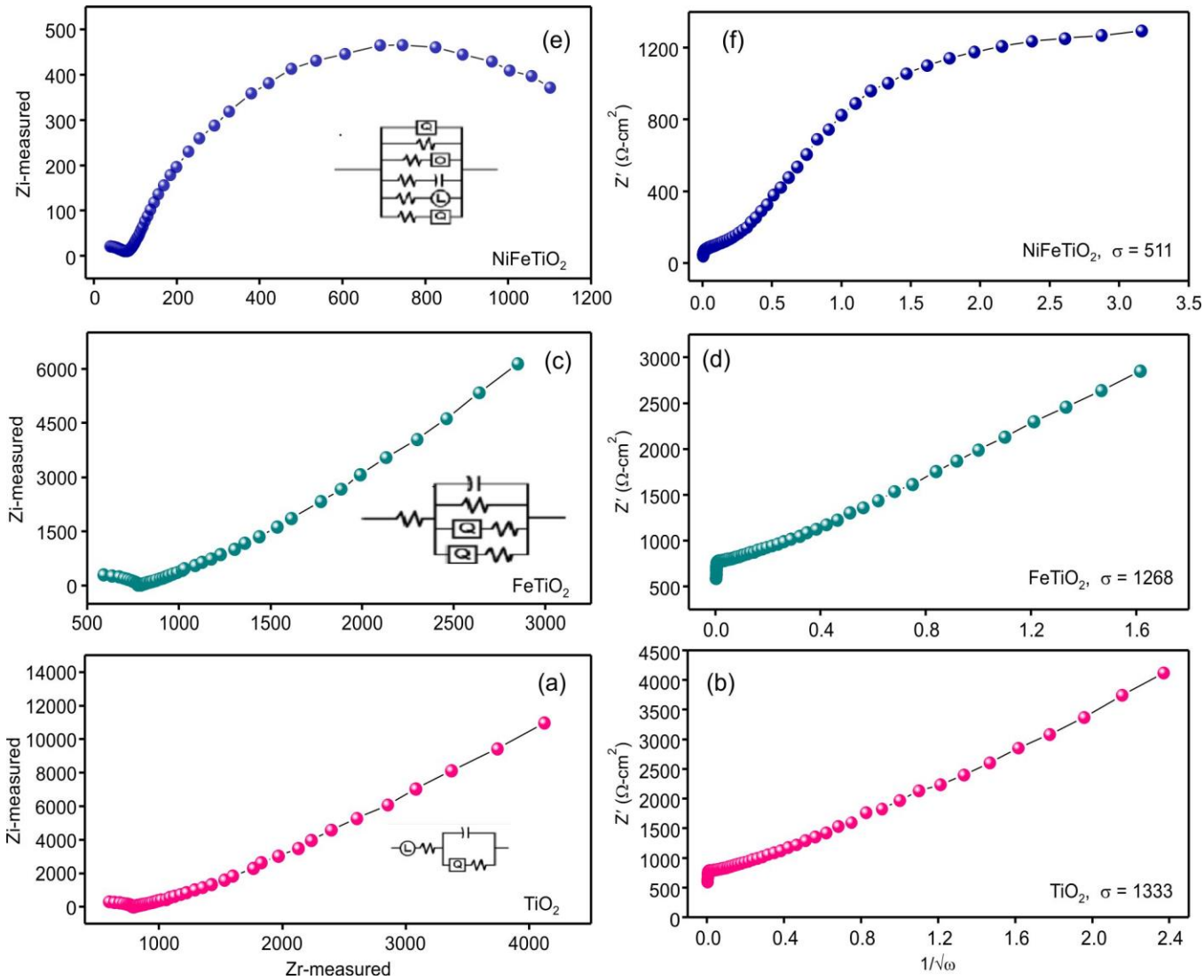

Fig. 6. EIS of TiO_2, Fe doped TiO_2, Ni and Fe co-doped TiO_2 NPs

tion observed for the NiFe-doped sample implies greater capacitance relative to pure TiO_2 and Fe doped TiO_2. Overall, the GCD results for TiO_2, Fe doped TiO_2, Ni and Fe co-doped TiO_2 nanoparticles demonstrate impressive capacitive characteristics with excellent reversibility and rate performance.

In addition, eqn. 4 was used to estimate the specific capacitance.

$$C_{sp} = \frac{A}{2mk\Delta V} \quad (4)$$

where A is the integrated area under the curve; m stands for the mass of electrode material; k corresponds to the scan rate; and ΔV signifies the voltage range and indicates the applied voltage window. The specific capacitance (C_{sp}) values were found to be 14 F g^{-1} for pure TiO_2, 67 F g^{-1} for Fe-doped TiO_2 and 140 F g^{-1} for Ni and Fe co-doped TiO_2. This trend reflects the well-known relationship between reduced particle size and enhanced electrochemical performance [35].

The performance of capacitive materials in battery research is generally assessed through their energy and power densities, as calculated using eqns. 5 and 6. Table-3 summarises the energy and power density values for TiO_2, Fe doped TiO_2, Ni and Fe co-doped TiO_2 nanoparticles. Fig. 8 shows the cycle stability and Coulombic efficiency of Ni and Fe co-doped TiO_2.

TABLE-3
ENERGY AND POWER DENSITIES OF TiO_2, Fe DOPED TiO_2, Ni AND Fe co-DOPED TiO_2 NPs

Samples	Energy density (Wh kg^{-1})	Power density (Kw kg^{-1})
TiO_2	18.82	36
$FeTiO_2$	134	44
$NiFeTiO_2$	280	54

The comparison of diverse synthesis techniques, electrolyte systems, specific capacitance, retention capabilities and cycle numbers are reported in Table-4.

$$\text{Energy density (E)} = \frac{1}{2C_{sp}(\Delta V)^2} \quad (5)$$

$$\text{Power density (P)} = \frac{E}{\Delta t} \quad (6)$$

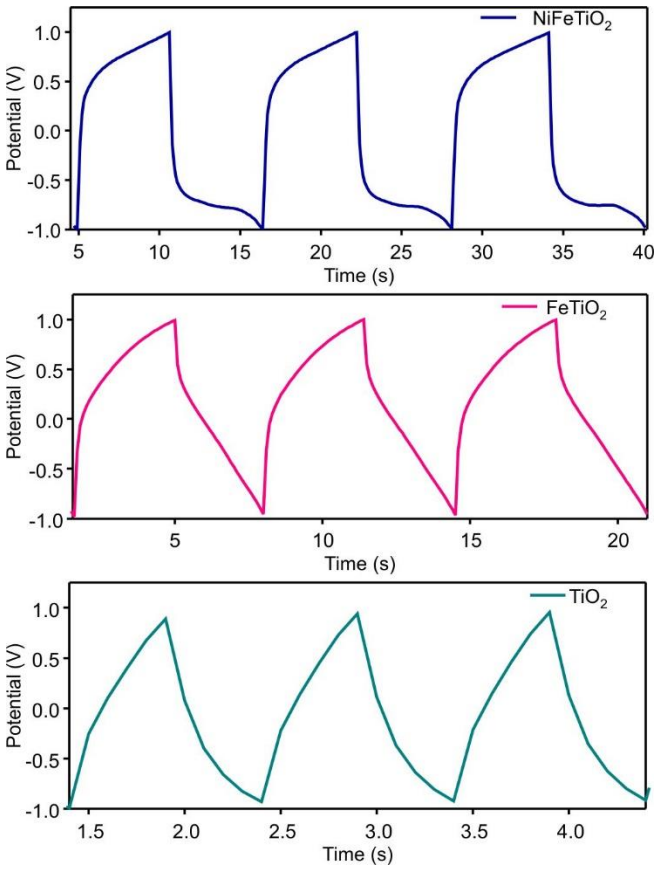

Fig. 7. GCD studies of TiO_2, Fe doped TiO_2, Ni and Fe co-doped TiO_2 NPs

Conclusion

In this work, Ni and Fe co-doped TiO_2 nanomaterials were synthesised through combustion method, utilising aloe vera gel as a sustainable fuel. This method produced smaller crystal structures and introduced defects into the TiO_2 lattice, as shown by XRD and Raman spectroscopy. Surface morphology observed through SEM showed reduced particle size along with improved dispersion. Addition of Ni and Fe created many active sites and oxygen vacancies, which improved the material's ability to store and move charge. Electrochemical tests showed the co-doped materials had higher capacitance, better energy storage and lower resistance than undoped TiO_2. The enhanced performance stemmed from a combination of double-layer capacitance and pseudocapacitive behaviour, delivering excellent stability and efficiency. Fe-doped and NiFe co-doped TiO_2 nanomaterials exhibited a distinct shift from surface-controlled to diffusion-limited charge storage, as indicated by reduced β-values. This transformation contributed to improved energy storage capabilities, making these materials well-suited for hybrid supercapacitors and battery-type applications. Compared to pure TiO_2, the doped electrodes showed higher energy capacity, faster charge/discharge response and outstanding cycling durability, underscoring their potential in next-generation energy storage systems. Overall, this green synthesis technique demonstrates that plant-based co-doping is a promising way to create high-performing, sustainable materials for future energy storage and supercapacitor applications.

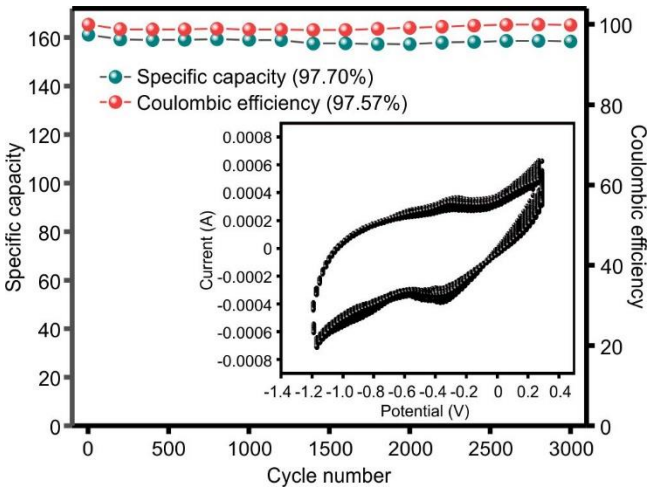

Fig. 8. Cycle stability and coulombic efficiency Ni and Fe co-doped TiO_2 NPs

ACKNOWLEDGEMENTS

This work was funded by the seed grant (File No: RI&C/Funded Project/SI-3 & 4 dated 08/11/2021) Presidency University, Bangalore, India.

TABLE-4
COMPARISON OF PREPARATION METHODS, ELECTROLYTE SOLUTIONS, SPECIFIC CAPACITANCE, CAPACITIVE RETENTION AND CYCLE NUMBERS

Materials	Preparation method	Electrolyte	Specific capacitance (F g^{-1})	Retention (%)	Cycle number	Ref.
Ni^{2+} doped $SrTiO_3$ nanoparticles	Ball milling method	3 M KOH	142	86	3000	[36]
Ni doped TiO_2 nanowires	Electrospinning	3 M KOH	200	100	5000	[37]
rGO nanosheets with NiO and TiO_2	Solvothermal	1 M KOH	793.6	89.37	5000	[38]
SnS@Ni/SnO_2	Hydrothermal process	1 M KOH	157	88	4000	[39]
rGO/NiO@TiO_2-RNT	Hydrothermal technique	1 M KOH	325	83	5000	[40]
Ni-Mn-oxide	Wet chemical synthesis	1 M Na_2SO_4	269	97	3000	[41]
Ni-MOF	Chemical oxidation method	KOH/ $K_4Fe(CN)_6$	154.3	90	3000	[42]
NCOPS	Hydrothermal		2915.6	80.39	4000	[43]
Ni-doped $AgFeO_2$	Precipitation method	3 M KOH	339.08	84	1000	[44]
NiFe co-doped TiO_2	Solution combustion method	1 M Na_2SO_4	140	97.57	3000	Present work

CONFLICT OF INTEREST

The authors declare that there is no conflict of interests regarding the publication of this article.

DECLARATION OF AI-ASSISTED TECHNOLOGIES

During the preparation of this manuscript, the authors used an AI-assisted tool(s) to improve the language. The authors reviewed and edited the content and take full responsibility for the published work.

REFERENCES

1. G. Yu, X. Xie, L. Pan, Z. Bao and Y. Cui, *Nano Energy*, **2**, 213 (2013); https://doi.org/10.1016/j.nanoen.2012.10.006
2. M.I. Rafiq, T. Farid, J. Zhou, A. Ali, J. Tang and W. Tang, *J. Alloys Compd.*, **811**, 151858 (2019); https://doi.org/10.1016/j.jallcom.2019.151858
3. A. Roy, A. Ray, P. Sadhukhan, S. Saha and S. Das, *Mater. Res. Bull.*, **107**, 379 (2018); https://doi.org/10.1016/j.materresbull.2018.08.013
4. A. Ray, A. Roy, S. Bhattacharjee, S. Jana, C.K. Ghosh, C. Sinha and S. Das, *Electrochim. Acta*, **266**, 404 (2018); https://doi.org/10.1016/j.electacta.2018.02.033
5. P. Maji, A. Ray, P. Sadhukhan, A. Roy and S. Das, *Mater. Lett.*, **227**, 268 (2018); https://doi.org/10.1016/j.matlet.2018.05.101
6. Y. Yang, R. Wang, Z. Shen, Q. Yu, R. Xiong and W. Shen, *Adv. Appl. Energy.*, **11**, 100146 (2023); https://doi.org/10.1016/j.adapen.2023.100146
7. S. Wodyk, M. Wieczorek, P. Witaszek and R. Poliszkiewicz, *Energy Rep.*, **9**, 106 (2023); https://doi.org/10.1016/j.egyr.2023.05.091
8. S.A. Al Kiey and M.S. Hasanin, *Environ. Sci. Pollut. Res. Int.*, **28**, 66888 (2021); https://doi.org/10.1007/s11356-021-15276-5
9. Z. Fei, Y. Su, Y. Zha, X. Zhao, Q. Meng, P. Dong and Y. Zhang, *Chem. Eng. J.*, **464**, 142534 (2023); https://doi.org/10.1016/j.cej.2023.142534
10. M. Tebyetekerwa, I. Marriam, Z. Xu, S. Yang, H. Zhang, F. Zabihi, R. Jose, S. Peng, M. Zhu and S. Ramakrishna, *Energy Environ. Sci.*, **12**, 2148 (2019); https://doi.org/10.1039/C8EE02607F
11. P. Poizot, J. Gaubicher, S. Renault, L. Dubois, Y. Liang and Y. Yao, *Chem. Rev.*, **120**, 6490 (2020); https://doi.org/10.1021/acs.chemrev.9b00482
12. T. Munawar, S. Manzoor, F. Mukhtar, M.S. Nadeem, A.G. Abid, M.N. Ashiq and F. Iqbal, *J. Mater. Sci.*, **57**, 11852 (2022); https://doi.org/10.1007/s10853-022-07390-7
13. M.Z.U. Shah, J. Feng, F. BiBi, M. Sajjad, M.T. Qureshi, A. Shah, M.S. Shah, A.M. Khaled and M.S. Salem, *J. Alloys Compd.*, **1013**, 178548 (2025); https://doi.org/10.1016/j.jallcom.2025.178548
14. N. Cherupurakal, R. Krishnapriya, A. Bojarajan, T. Ramachandran, S. Sangaraju, M.S. Mozumder and A.-H.I. Mourad, *Mater. Renew. Sustain. Energy*, **13**, 361 (2024); https://doi.org/10.1007/s40243-024-00269-4
15. S. Lou, Y. Zhao, J. Wang, G. Yin, C. Du and X. Sun, *Small*, **15**, 1904740 (2019); https://doi.org/10.1002/smll.201904740
16. K. Raju, S. Rajendran, T.K.A. Hoang, D. Durgalakshmi, J. Qin, D.E. Diaz-Droguett, F. Gracia and M.A. Gracia-Pinilla, *J. Power Sources*, **466**, 228305 (2020); https://doi.org/10.1016/j.jpowsour.2020.228305
17. X. Liu, L. Xu, Y. Huang, C. Qin, L. Qin and H.J. Seo, *Ceram. Int.*, **43**, 12372 (2017); https://doi.org/10.1016/j.ceramint.2017.06.103
18. H. Khan and I.K. Swati, *Ind. Eng. Chem. Res.*, **55**, 6619 (2016); https://doi.org/10.1021/acs.iecr.6b01104
19. S.T. Almutairi, *Heliyon*, **10**, e35400 (2024); https://doi.org/10.1016/j.heliyon.2024.e35400
20. M.I. Hossain, F.K. Tareq and S. Rudra, *Electrochem. Commun.*, **176**, 107942 (2025); https://doi.org/10.1016/j.elecom.2025.107942
21. M.R.A. Kumar, B. Abebe, H.P. Nagaswarupa, H.C.A. Murthy, C.R. Ravikumar and F.K. Sabir, *Sci. Rep.*, **10**, 1249 (2020); https://doi.org/10.1038/s41598-020-58110-7
22. Y. Masuda and K. Kato, *J. Ceram. Soc. Jpn.*, **117**, 373 (2009); https://doi.org/10.2109/jcersj2.117.373
23. J. Xing, Y.H. Li, H.B. Jiang, Y. Wang and H.G. Yang, *Int. J. Hydrogen Energy*, **39**, 1237 (2014); https://doi.org/10.1016/j.ijhydene.2013.11.041
24. L. Zhu, Q. Lu, L. Lv, Y. Wang, Y. Hu, Z. Deng, Z. Lou, Y. Hou and F. Teng, *RSC Adv.*, **7**, 20084 (2017); https://doi.org/10.1039/C7RA00134G
25. T. Tong, J. Zhang, B. Tian, F. Chen and D. He, *J. Hazard. Mater.*, **155**, 572 (2008); https://doi.org/10.1016/j.jhazmat.2007.11.106
26. I. Ganesh, A.K. Gupta, P.P. Kumar, P.S.C. Sekhar, K. Radha, G. Padmanabham and G. Sundararajan, *Scient. World J.*, **2012**, 127326 (2012); https://doi.org/10.1100/2012/127326
27. A. El Mragui, Y. Logvina, L. Pinto da Silva, O. Zegaoui and J.C.G. Esteves da Silva, *Materials*, **12**, 3874 (2019); https://doi.org/10.3390/ma12233874
28. A.G. Ilie, M. Scarisoareanu, I. Morjan, E. Dutu, M. Badiceanu and I. Mihailescu, *Appl. Surf. Sci.*, **417**, 93 (2017); https://doi.org/10.1016/j.apsusc.2017.01.193
29. Alamgir, W. Khan, S. Ahmad, M. Mehedi Hassan and A.H. Naqvi, *Opt. Mater.*, **38**, 278 (2014); https://doi.org/10.1016/j.optmat.2014.10.054
30. Y. Zhang, X. Li, Z. Li and F. Yang, *J. Energy Storage*, **86**, 111122 (2024); https://doi.org/10.1016/j.est.2024.111122
31. J.C. Martins, J.C. de M. Neto, R.R. Passos and L.A. Pocrifka, *Solid State Ion.*, **346**, 115198 (2020); https://doi.org/10.1016/j.ssi.2019.115198
32. S.S. Suranshe, A. Patil, T. Deshmukh and J. Chavhan, *Electrochim. Acta*, **450**, 142277 (2023); https://doi.org/10.1016/j.electacta.2023.142277
33. E. Krishnakanth, P. Mohan Kumar, P.R. Deepthi, A. Sukhdev and C.S. Ramesh, *Ceram. Int.*, **50**, 46548 (2024); https://doi.org/10.1016/j.ceramint.2024.09.007
34. M. Priyanka, Y.S. Vidya, H.C. Manjunatha, R. Munirathnam, S. Manjunatha, M. Shivanna, S. Kumar and E. Krishnakanth, *Mater. Sci. Eng. B*, **322**, 118503 (2025); https://doi.org/10.1016/j.mseb.2025.118503
35. K. Chalvan, Y.S. Vidya, H.C. Manjunatha, N. Dhananjaya, R. Munirathnam, S. Manjunatha, M. Shivanna, S. Kumar, E. Krishnakanth, K. Manjunatha and S.Y. Wu, *Inorg. Chem. Commun.*, **164**, 112346 (2024); https://doi.org/10.1016/j.inoche.2024.112346
36. C.I. Priyadharsini, G. Marimuthu, T. Pazhanivel, P.M. Anbarasan, V. Aroulmoji, S. Prabhu and R. Ramesh, *Ionics*, **26**, 3591 (2020); https://doi.org/10.1007/s11581-019-03412-8
37. S.G. Krishnan, P.S. Archana, B. Vidyadharan, I.I. Misnon, B.L. Vijayan, V.M. Nair, A. Gupta and R. Jose, *J. Alloys Compd.*, **684**, 328 (2016); https://doi.org/10.1016/j.jallcom.2016.05.183
38. S. Sundriyal, M. Sharma, A. Kaur, S. Mishra and A. Deep, *J. Mater. Sci. Mater. Electron.*, **29**, 12754 (2018); https://doi.org/10.1007/s10854-018-9393-5
39. D. Singh, M. Pershaanaa, N.K. Farhana, S. Bashir, K. Ramesh and S. Ramesh, *BMC Chem.*, **18**, 196 (2024); https://doi.org/10.1186/s13065-024-01307-y
40. S. Harini, S.V. Anto Feradrick, R.M. Victor Antony and J. Madhavan, *J. Appl. Electrochem.*, **55**, 797 (2025); https://doi.org/10.1007/s10800-024-02200-1
41. A. Ray, S. Saha, M. Ghosh, S. Roy Chowdhury, T. Maiyalagan, A. Roy, S.K. Bhattacharya and S. Das, *Langmuir*, **35**, 8257 (2019); https://doi.org/10.1021/acs.langmuir.9b00955
42. Z. Qin, Y. Xu, L. Liu, M. Liu, H. Zhou, L. Xiao, Y. Cao and C. Chen, *RSC Adv.*, **12**, 29177 (2022); https://doi.org/10.1039/D2RA04939B
43. J. Wu, F. Yan, Z. Huang, J. Liu, H. Huang, Y. Liang, J. Li, F. Yuan, X. Liang, W. Zhou and J. Guo, *J. Energy Storage*, **97**, 112958 (2024); https://doi.org/10.1016/j.est.2024.112958
44. C. Veann, W. Limphirat, R. Maensiri and S. Maensiri, *J. Energy Storage*, **110**, 115249 (2025); https://doi.org/10.1016/j.est.2024.115249